ENGINE ANALYSIS AND IMPROVEMENTS

Aero-thermal Analysis and Characterization of Fine Wire Thermocouple Probes

Laura Villafañe

Turbomachinery and Propulsion Department, von Karman Institute for Fluid Dynamics, Belgium, laura.villafane@vki.ac.be

Supervisor: Guillermo Paniagua

Associate Professor, Turbomachinery and Propulsion Department, von Karman Institute for Fluid Dynamics, Belgium, paniagua@vki.ac.be.

University Supervisor: Jose María Desantes

Full Professor, Máquinas y Motores Térmicos, Universitat Politècnica de València, Spain

Abstract

Thermocouple probes for accurate gas temperature measurements require specific designs optimized for a given application and precise characterization of the probe performances. In the present investigation a numerical procedure is proposed that outperforms previous experimental approaches to analyze the thermocouple response and the different sources of temperature error. Results from conjugate heat transfer simulations on different shielded thermocouples are presented, that provide information of the influence of the design parameters on the error sources.

Keywords: thermocouples, conjugate heat transfer (CHT), recovery factor, conduction effects, response time, transfer function

1. Introduction

Innovative finned heat exchangers are being studied in the bypass of gas turbine engines to improve their thermal management. In this context, high fidelity temperature measurements are needed along the three dimensional transonic flow within an intermittent facility, interacting with an array of fins.

In the present investigation numerical simulations are performed to study the steady and unsteady heat fluxes within a temperature probe. A numerical procedure to analyze the response of thermocouple probes is proposed. Its application to shielded thermocouples allows investigating the distinct contributions that deviate the measurement from the real gas temperature, and their evolution with time.

Multiple attempts to provide correction factors for standard thermocouple designs can be found in the literature [1; 2; 3]. It is a common practise to report over-all recovery factors experimentally determined as an indicator of the temperature error of a thermocouple. While useful in comparing probe designs, they account for the total effect of radiation, conduction and convection on the probe on a given flow environment, within a correction coefficient in which not all the temperature errors have the same weight under different experimental conditions. The variability of the heat fluxes with the environment and probe design, requires each thermocouple to be carefully designed and calibrated. However, precise corrections from experimental probe calibrations are impractical. During calibration not only the flow conditions need to be replicated but also the thermal interactions between the probe and the test bench. Furthermore, the precision to reproduce and to characterize the calibration environment determines the accuracy of the corrections.

The numerical characterization of the probes excells previous experimental experiences in accuracy and simplicity. The presented numerical methodology allows understanding and quantifying the design parameters required to achieve precise gas temperature measurements. Adiabatic recovery factors, conduction error estimations and response time characteris-

tics are determined for a shielded probe with different values of wire diameter, thermocouple wire properties and boundary conditions at the thermocouple wire support. The present numerical approach may be coupled with optimizers to facilitate and improve the design of a probe for a certain application.

2. Thermocouple Probe Design

2.1. Application

To study a heat exchanger to be mounted downstream of the engine's inlet fan, a measurement test bench was prepared. A transonic wind tunnel with a distorted annular sector, helicoidal test section was manufactured. Total flow temperature measurements are to be performed in this intermittent wind tunnel discharging to the atmosphere from a pressurized vessel. The flow temperature decreases during a test run due to the flow expansion in the reservoir. Flow temperature traverses are to be recorded along the test section of transversal area about 0.013 m^2. High-frequency response is required in order to allow fast traverses. A rake of temperature probes allows to maximize the measurement locations in a test. Precise characterization of the probe response is necessary to synchronize all readings, as well as to accurately analyze the heat exchanger efficiency.

2.2. Pre-existent design rules

The temperature of a thermocouple junction is the result of the energy balance including the convective heat flux between the junction and the surrounding gas, radiation to the surrounding walls, and conductive flux to the wire. The balance is different for each probe and each condition. The measured temperature would be equal to the total flow gas temperature in the absence of radiative heat fluxes, conductive flux to the thermocouple support and dissipation of kinetic energy in the boundary layer.

General design rules provide advises to reduce the temperature error sources. A shield is recommended in order to decrease the error caused by the dissipation of kinetic energy in the boundary layer around the junction (often called velocity error). The shield also provides structural resistance in high velocity flows and reduces radiation effects. However decreasing the velocity of the flow decreases the convective heat transfer, penalizing the conduction error and the response time. Thus, the internal velocity must be kept as high as allowable. The internal velocity is function of the vent hole to inlet ratio. The junction position within the shield is a compromise between non-aligned entrance flow effects, and flow alteration due to convective heat transfer to the shield. Recommended values are given by Rom and Kronzon [2], Saravanamuttoo [4] and Glawe et al. [1]. The wires within the shield can be placed parallel or perpendicular to the flow. In the first case, the length of the wires is limited to prevent wire bending. In the second, the length is limited by the shield diameter.

Conduction errors can be estimated from the simplified solution of the 1D energy equation for a wire element dx, (Eq.1), considering symmetry boundary condition $\partial T/\partial x = 0$ at the junction ($x = 0$), and isothermal temperature $T_w = T_{sp}$ at the support of the wire ($x = l$). Eq. 2 provides a simplified solution particularized for the junction. The assumption of constant gas temperature and constant convection coefficient h, neglects the effect of the real flow temperature differences along the wire.

$$h(T - T_g)\pi d_w dx = k\frac{\partial^2 T}{\partial x^2}\pi\frac{d_w^2}{4}dx \tag{1}$$

$$T_{ad} - T_j = \frac{T_{ad} - T_{sp}}{\cosh(l\sqrt{\frac{4h}{k_w d_w}})} = \frac{T_{ad} - T_{sp}}{\cosh(l/l_c)} \tag{2}$$

Let us consider the total temperature of the gas T_g, equal to the junction recovery temperature T_{ad}, namely the total temperature in the absence of velocity error. Design rules derived from this simplified solution recommend to have high values of h (high velocities), high l/d_w ratios, low conductivity wire materials, and support temperatures close to gas temperature. Petit et al. [5] suggest that the ratio l/l_c should not be smaller than 5.

The contribution of the error due to radiation is generally important at high flow temperatures. The simplified relationship (Eq.3) considering the most adverse conditions with unity view factor and equal conductive and radiative areas yielded a negligible error, lower than $4 \cdot 10^{-4}$%, about 1 mK.

$$T_0 - T_j = \frac{K_R\sigma\epsilon A_R(T_j^4 - T_W^4)}{hA_c} \tag{3}$$

In flow temperature transients the energy balance at the thermocouple junction or on a dx at any position along the wire can be expressed by Eqs. 4. As in the steady case, T_g is considered equal to T_{ad} in the absence of velocity errors.

$$S_j h_j (T_g - T_j) + \frac{\pi}{2} d_w^2 k_w \left(\frac{\partial^2 T_w}{\partial x^2}\right)|_{x=0} = \rho_j C_{p,j} V_j \frac{\partial T_j}{\partial t}$$
$$h_w (T_g - T_w) + \frac{d_w}{4} k_w \left(\frac{\partial^2 T_w}{\partial x^2}\right) = \rho_w C_{p,w} \frac{d_w}{4} \frac{\partial T_w}{\partial t} \quad (4)$$

In the case of uniform temperature on the junction, constant heat transfer coefficient independent with time, and no heat transfer by conduction between the junction and the adjacent wire, the thermocouple response to a temperature step is a first order system, Eq. 5. The assumption of first order system would be also valid for the assembly wire and junction if their diameters are identical, there are no radial or longitudinal temperature gradients, no conductive heat transfer to the supports, and the heat transfer coefficient is constant in time and along the length of the wire. Eq. 5, provides the time constant.

$$T_g = T_j + \tau \frac{\partial T_j}{\partial t}, \quad \text{with} \quad \tau_j = \frac{\rho_j C_{p_j} V_j}{h_j S_j}; \quad \tau_w = \frac{\rho_w C_{p_w} d_w^2}{4 k_g N u_w} \quad (5)$$

2.3. Shielded probe design

The temperature probe consists of a rake of five shielded thermocouples. Minimization of blockage effects given the small transversal area of the test section is considered, while preserving the structural resistivity of the whole rake. The geometric characteristics of the temperature probe heads are sketched in Fig. 1.

A type T thermocouple (copper-constantan) is placed perpendicular to the flow with a total length equal to the internal shield diameter, 2 mm. This wire configuration is intended to avoid wire bending at high velocities. Ratios $(l/d)_w$ of 79 are obtained with wires of 25.4 μ m diameter. The ratio weld-bead to wire diameter measured after probe manufacturing is about 2.7. The shield diameter is a compromise between the blockage minimization, wire structural resistivity and limitation of conduction errors. The shield is made of polycarbonate, chosen for its low conductivity. In agreement with the values recommended in the literature [1], [2], [4], the inlet/outlet area ratio is 4 and the junction is placed at 1/2 internal shield diameters from the entrance.

3. Methodology of the aerothermal study.

The transfer function of a thermocouple probe can be obtained by evaluating the response to a temperature step. Experimentally, the accuracy of the temperature corrections requires a precise control of the gas temperature excitation and test conditions.

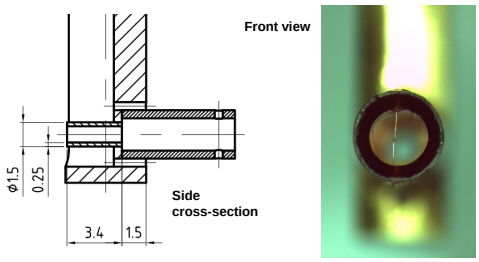

Figure 1: Shielded thermocouple probe.

At the transonic conditions of interest, the characteristic time for the flow to develop around the thermocouple is two orders of magnitude smaller than the characteristic time of the thermal transient in the thermocouple wires. This allows to perform simulations in two stages. First of all, a steady simulation is solved to establish the flow around the probe considered isothermal. This steady solution is referred as the reference case. Secondly a conjugate heat transfer (CHT) simulation is initiated from the reference solution, solving also the energy balances within the solid domains of the thermocouple. This second stage is ran in steady or transient state depending on whether the interest is focused on the steady temperature errors or on the transient behavior. In the latter case, the result is the response of the thermocouple to a temperature step. The decomposition in two stages highly reduces the computational cost.

This methodology allows the analysis of the heat fluxes within the thermocouple and the influence of the flow environment, probe geometry and wire materials.

4. Numerical Tools.

4.1. Computational domain and solver

The shielded thermocouple head is modeled in a 3D domain constituted by a quarter of a cylinder thanks to the existence of two symmetry planes on the probe geometry. The grid extends 6 shield diameters in the radial direction and in the axial direction upstream of the probe, and 10 diameters downstream. The three solid parts (shield , wire and junction) are meshed independently and concatenated to the gas domain mesh in the NS solver used. The gas hybrid 3D mesh composed by about 1.75 million cells is shown in Fig. 2.

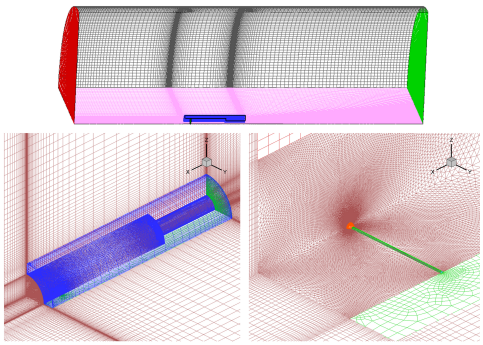

Figure 2: Computational domain. Left: TC shield view. Right: TC wire and junction.

The grid is refined along the walls of the solid parts and specially around the thermocouple wire and junction.

The Reynolds Averaged Navier Stokes solver employed was CFD++ (v.8.1). The k-epsilon turbulence model was considered, with initial values of k and epsilon estimated as a function of the free stream nominal velocity, with a free-stream turbulence level of 1% and a turbulence length scale based on the tube inner diameter. Values of y^+ in the vicinity of the thermocouple junction are lower than 0.3, and lower than 0.5 along the wire. For the steady simulations convergence is achieved after 1000 iterations , 5.5 hours CPU time in 8 parallel Intel Core 2 Quad Q9400 (2.66 GHz) machines. For the transient simulations the temperature of the solids is released by changing the boundary conditions to CHT. The integration time step is adjusted as function of the temperature gradients starting from 0.1ms. The CPU time required to reach steady junction temperature when CHT is activated in all the solid domains, varies depending on the wire conductivity. Approximately 1000 iterations with different time steps are required in a low conductive material, involving 51 hours CPU time running in 8 parallel machines, while up to 6000 iterations are required for a high conductive wire.

4.2. Numerical test conditions

Nominal flow conditions for the simulations correspond to inlet boundary conditions $T_s = 273.22K$, $P_s = 101325Pa$, $V_\infty = 231.12m/s$, and $P_s = 101325Pa$ at the domain outlet. Different Mach and Reynolds numbers were tested for the geometrical configuration corresponding to the design geometry.

Three geometrical configurations were analyzed (Table. 1), the reference design is henceforth referred

Table 1: Probe geometric configurations.

	Geom 1	*Geom 2*	*Geom 3*
$l, [mm]$	1	1	1
$d_w, [mm]$	0.0254	0.0508	0
$d_j, [mm]$	0.07	0.14	0.07

Geom 1. The shield is the same in the three cases. The modified parameter is the wire diameter, doubled in *Geom 2* where the ratio junction to wire diameter has been kept constant. *Geom 3* refers to the study of a spherical junction with infinitely thin wires.

Heat loss through the wires to the support is function of the wire dimensions, material conductivity, support temperature and convective heat transfer along the wire. In order to study the so called conduction effects different wire materials and boundary conditions at the support are analyzed for the configurations *Geom 1* and *Geom 2*. In all cases the shield material is polycarbonate and the junction properties are an average of the two materials of type T thermocouple (copper and constantan). Two other materials are also considered in the study: Nicrosil and an ideal material with low conductivity, referred as Ideal (Table 2). The different support boundary conditions tested were:

(a) The shield-support behaves as an adiabatic solid,
(b) the shield is isothermal at 300 K,
(c) CHT on the shield.

5. Steady Temperature Effects

5.1. Global Temperature Correction

The junction temperature results as the balance between the convective heat fluxes between gas-junction and gas-wire, and the conductive flux between junction and wire influenced at the same time by the conductive heat flux between the wire and its support. If those effects were decoupled, individual error equations could be used to estimate the deviation of the measured temperature. However, in practical applications the junction temperature must be evaluated by the simultaneous solution of the different heat flux rates [6].

The overall recovery factor Z (Eq. 6), indication of the difference between the measured temperature (T_j) and the total temperature of the gas (T_0), can be decomposed into several contributions. The first term

Table 2: Material properties of thermocouple wires. Evaluated at 23°C.

	Copper	Constantan	Nicrosil	Ideal	Polycarbonate
K, [W m^{-1} K^{-1}]	401	19.5	13	1	0.2
ρ, [kg m^{-3}]	8930	8860	8530	8860	1210
C_p, [J kg^{-1} K^{-1}]	385	390	460	390	1250

(a) is the velocity error, related to the adiabatic recovery factor. The second term (b), takes into account the temperature error due to conduction and convection of heat in the wire in contact with the junction, for a given temperature of the support-shield (T_{sp}). The last term (c) collects the adiabatic recovery factor of the shield and the conduction effects between the shield, the probe stem, and the external probe support. The numerical method applied allows analyzing separately each contribution.

$$(1-Z) = \frac{T_0 - T_j}{T_0 - T_\infty} = \overbrace{\frac{T_0 - T_{ad}}{T_0 - T_\infty}}^{a} + \overbrace{\frac{T_{ad} - T_j}{T_{ad} - T_{sp}}}^{b} \cdot \overbrace{\frac{T_{ad} - T_{sp}}{T_0 - T_\infty}}^{c} \tag{6}$$

5.2. Velocity error

Temperature probes are intended to measure the gas total temperature, i.e. the temperature that the gas would attain if it is brought to rest through an isentropic process. However, in real gases (where the Prandtl number differs from one), frictional heat is generated within the boundary layer, hence the conversion of kinetic energy into thermal enthalpy is not perfect. The recovery factor, Eq. 7, represents the amount of kinetic energy recovered by the gas, where T_{ad} is the temperature of the surface of the junction in case it would behave as an adiabatic body, and V is the reference flow velocity upstream of the junction. The recovery factor is function of the geometry of the immersed body and the Prandtl number of the fluid. Experimental values of adiabatic recovery factor determined by different authors [7; 8; 9] were collected by Moffat [10] for bare wires parallel and normal to the flow.

$$r = \frac{T_{ad} - T_s}{V^2/2C_p} = 1 - \frac{T_0 - T_{ad}}{V^2/2C_p} \tag{7}$$

For shielded thermocouples behaving as adiabatic bodies, the term (a) in Eq. 6 represents an overall adiabatic recovery factor, related to r as expressed by Eq.8. The velocity upstream of the junction within the shield (V) is different from the free stream flow velocity (V_∞).

$$Z_a = \frac{T_{ad} - T_s}{V_\infty^2/2C_p} = 1 - \frac{T_0 - T_{ad}}{V_\infty^2/2C_p} = 1 - (1-r)(V_{int}^2/V_\infty^2) \tag{8}$$

Experimental determination of recovery factors is impractical since the junction temperature needs to be measured with great accuracy, and ensuring negligible influence of conduction along the wires to the supports, so that the junction behaves as an adiabatic body. Steady simulations at different flow velocities allow determining both r and Z_a and their sensibility to flow Mach and Reynolds numbers. Wire and shield are considered adiabatic solids in the computations and CHT is solved at the junction, which temperature is considered T_{ad}.

Computations have been also performed considering all the solid boundaries adiabatic, junction included. The average temperature on the junction adiabatic surface $T_{ad,m}$ has been compared with the junction temperature derived when CHT is solved on it, for the same flow conditions. Temperature differences observed, lower than 0.004 % ($T_{ad,m} - T_{ad}/T_{ad,m}$), are explained by the junction heat capacity of the small junctions considered.

Figure 3(a) shows the evolution of the recovery factor r and the overall recovery factor Z_a, for three different Mach numbers at constant Reynolds number based on the wire diameter. The adiabatic recovery factor slightly increases when the flow Mach number, and thus the velocity within the shield (about six times slower than the external flow), increases. The results are in good agreement with the recovery values compiled in the work of Moffat [10]. The effect of increasing Reynolds number at constant Mach number is also indicated. For the same probe geometry *Geom 1*, at constant temperature and Mach number, an increase in the Reynolds number is due to an increase in static pressure, and its consequence is to slightly decrease the recovery factor. For the nominal flow conditions, increasing the diameter of the thermocouple wire and junction *Geom 2*, yields to an increase of the Reynolds number, and analogously a slight decrease of the recovery factor. The overall recovery factor presents the same tendency while being less sensitive to Mach and

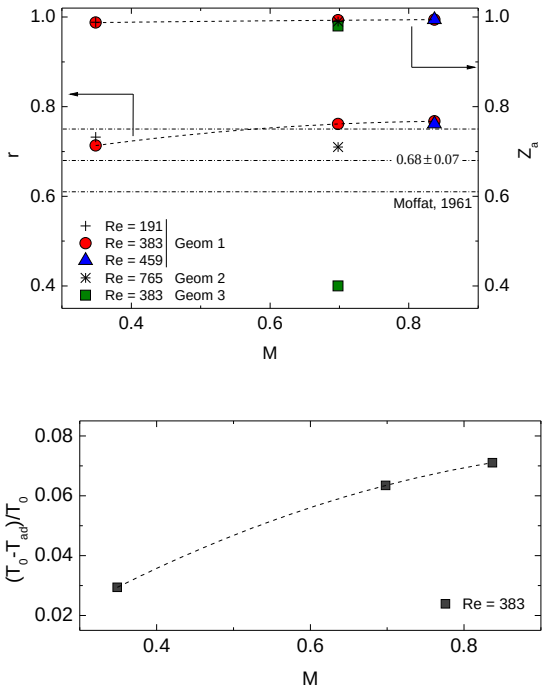

Figure 3: a) Recovery factors for different probe geometries, Mach and Reynolds numbers, b) Temperature error due to no isentropic flow deceleration

Reynolds variations.

Recovery factors have been computed likewise for *Geom 3*, providing lower values. The flow behavior around a sphere is clearly not similar to that around a thermocouple junction, neither to the flow parallel to a cylinder [10]. Comparison of the flow fields around the junction for *Geom 1* and *Geom 3*, shows a stronger flow deceleration in the first case forced by the presence of the wires. The thermal boundary layer around the junction in the presence of the wires is substantially thicker, and the transformation of the flow kinetic energy into thermal energy is more efficient.

Although the recovery factor increases with the Mach number, the kinetic velocity rises in a higher amount, thus the temperature error represented in Fig. 3(b) for the nominal flow conditions, also increases with velocity.

5.3. Conduction error

Free of velocity errors, the difference between the real junction temperature and the total temperature is the temperature error due to conduction, namely the product of terms (b) and (c) in Eq.6. In a well designed thermocouple, the junction temperature should be little sensitive to the support temperature, what is true when (b) is close to zero. In that case the overall contribution to the temperature error due to conduction would be negligible whatever the contribution of the term (c). In real applications term (b) is different to zero.

Term (b) reflects the influence of the conduction effects along the wire and those to the support, on the junction temperature. Its contribution can be expressed by the solution of the one dimensional energy equation, Eq.2. Thus, it decreases exponentially as the parameter l/l_c increases (for x$\geq$ 5, cosh x $\simeq$ 0.5e^x). Term (c) indicates the strength of the potential heat transfer between the thermocouple and the support. The lower temperature of the shield/support with respect to the total gas temperature in the absence of velocity error, $T_{ad} - T_{sp}$, drives the conduction to the wire. In the case the support would be perfectly isolated from external sources, it is function of the recovery factor of the complete shield/support. In reality, it is also function of the depth of immersion of the support on the flow, its geometry and thermal properties, and the external boundary condition of the probe.

The values of the parameter l/l_c for each material and each of the two geometries considered are indicated in Tab. 3. For the computation of l/l_c, Eq. 9, air conductivity is evaluated at the gas total temperature

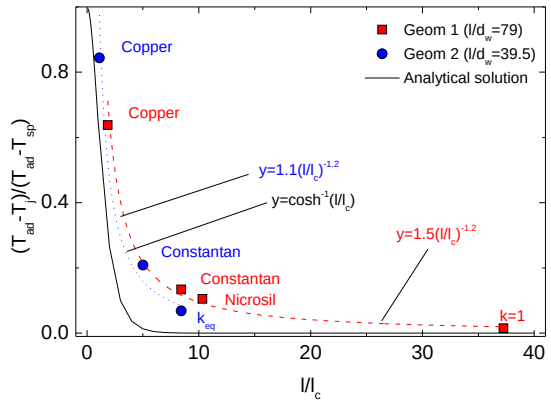

Figure 4: Ratio junction to support temperature deviations with respect to total temperature in function of the parameter l/l_c. Results from CHT simulations

[6], and the Nusselt number is derived from a correlation valid for wires perpendicular to the flow [10]: $Nu = (0.44 \pm 0.06)Re^{0.5}$.

$$\frac{l}{l_c} = l\sqrt{\frac{4h}{k_w d_w}} = \frac{2l}{d_w}\sqrt{\frac{Nuk_g}{k_w}} \tag{9}$$

Fig. 4 shows the non-dimensional conduction temperature error corresponding to term(b) in Eq.6. All results correspond to complete CHT simulations. The temperatures difference ratio is plotted versus the parameter l/l_c, which for a given probe geometry is only varied by a change in the wire material. The error decreases as the parameter l/l_c increases indicating that the junction temperature is less influenced by the conduction effects. The results show two slightly distinct trends for each l/d_w case that are best fitted by power laws with a common exponent coefficient of -1.2. The equivalent material, k_{eq}, corresponds to an hypothetical material with a conductivity such that the l/l_c value for *Geom*2 is equal to the l/l_c value for constantan wire and *Geom*1 ($k_{eq} = k_{const}\sqrt{2}/4$). At this l/l_c value (8.43), the contribution of conduction of term (b) is slightly smaller for *Geom*2. The analytical prediction (Eq.2) underestimates the results when compared with the numerical results. This discrepancy can be explained by the simplifications introduced in the analytical solution, especially the assumption of homogeneous gas temperature and heat transfer coefficient along the wire, and equal to the conditions at the junction. The parameter l/l_c is a good estimator of the conduction error, but inappropriate to establish a unique relation with the temperature error.

Figure 5(a) represents the global contribution to the conduction error computed for the reference probe ge-

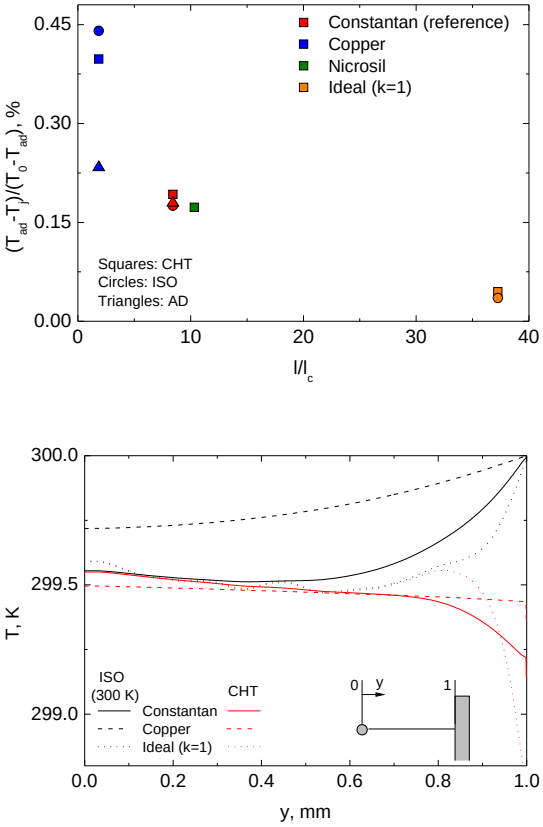

Figure 5: a)Overall temperature errors due to conduction in function of l/l_c, b)Wire temperature distributions

Table 3: Material parameters of thermocouple wires affecting conduction.

	Constantan	Copper	Nicrosil	Ideal	Equivalent
k, [kW m^{-1} K^{-1}]	19.5	401	13	1	6.89
l/l_c (Geom 1)	8.43	1.86	10.33	37.24	
l/l_c (Geom 2)	5.01	1.11	n.a.	n.a.	8.43

ometry (*Geom*1) for different materials. The figure compares for a given wire material and geometry, thus a given l/l_c, the variability of the temperature error due to the conditions at the shield/support. Fig. 5(b) displays the temperature distribution along the wire in the same conditions for three of the materials and two of the boundary conditions, adiabatic support and CHT within wire and support. The junction temperature ($y = 0$) is the same for the ideal wire ($l/l_c = 37$) independently of the conduction at the shield, with an overall conduction error about 0.04 %. The temperature at each position along the wire is less affected by the longitudinal conduction, hence by the shield temperature, and more by the convective heat flux. Thus the temperature distribution is able to reflect the non homogeneity of the gas temperature around the wire. The junction is only influenced by the wire temperature adjacent to it, and the effect of the shield temperature penetrates until the last 20% of the wire. In the case of constantan wire the temperature along the wire is affected by conduction to the shield to a higher extent. However, the temperature at the junction converges to almost the same value for the different boundary conditions. Overall conduction errors vary between 0.18 and 0.19 %. In the copper wire case, with a l/l_c about 2, conduction with the support influences the junction temperature in a higher degree. Errors vary between 0.23 and 0.45% depending on the support conditions.

The reference adiabatic temperature considered for the analysis of the conduction errors is that of the junction. However, due to the strong flow deceleration taking place around the wire in the vicinity of the junction, there is a less efficient flow deceleration in this region. Thus, the temperature recovered is lower when compared to the junction. This effect can be observed in Fig. 5(b) for the ideal wire distribution in which the temperatures at 10 to 20 % from the junction are slightly lower than at the junction. It explains also the slight difference between the junction temperatures for constantan and ideal material wires. The higher conductivity of constantan forces the junction to stabilize at the lower temperature of the wire in the vicinity, while for the ideal material the temperature at the junction rises to almost the adiabatic temperature.

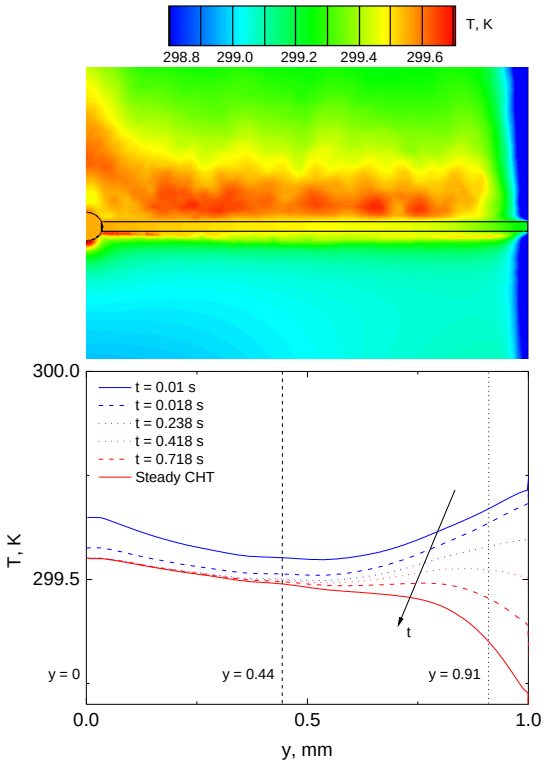

Figure 6: a)2D temperature contour, steady conditions. b) Evolution of constantan wire temperature distribution. CHT result

6. Transient Temperature Effects

The diffusive characteristics of the heat fluxes within the probe introduce a temperature lag on the junction temperature. The properties and geometry of the thermocouple wires affect the junction temperature evolution.

The numerical methodology applied in this study allows analyzing the temperature evolution on the complete probe in response to a temperature step. All the results correspond to the reference flow conditions and the initial temperature of the probe is T_i=300 K.

The temporal evolution of the temperature along the constantan wire for *Geom*1 is displayed in Fig.6. At

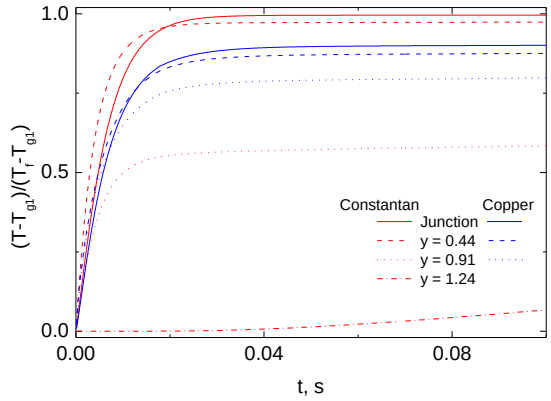

Figure 7: Temperature evolution at four control points on constantan and copper wires

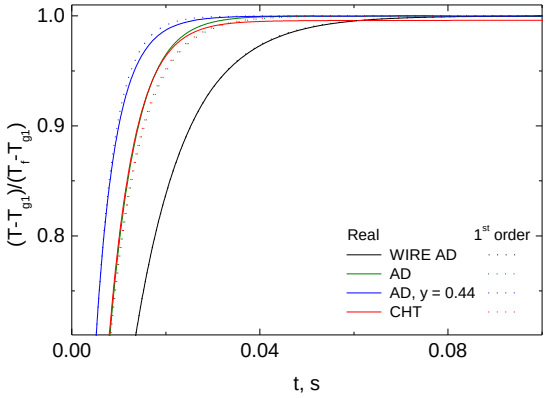

Figure 8: Comparison junction temporal evolutions with the correspondent first order.

each position along the wires, the rate of temperature change is different. The response time of the shield is much higher than that of the junction or wire due to its larger thermal inertia and lower thermal diffusivity a. Thus the part of the wire closer to the junction $y = 0$ reaches the final temperature faster than the part of the wire close to the shield/support due to its influence by conduction. Figure 7 shows the time temperature history at three wire positions and a point within the shield, for constantan and copper materials. The temperature traces are made non dimensional with their steady value in order to compare the response times, not taking into account the differences on the final temperature achieved.

All the temperature distributions, except that of the shield, show a fast initial temperature change, followed by a slower evolution. The fast initial temperature rise is dictated by the inertia of the junction or wire elements. The slow down is accentuated by the influence of the support at a certain position. In the constantan case the junction overpasses the conventional threshold of the 63.2 % of the response in 6.5 ms, and achieved the 90% of the final temperature in 18 ms. The temperature at $y = 0.44$mm shows a faster initial rise due to the lower thermal inertia of a wire element when compared with the junction, of bigger volume. However the convergence to the final temperature takes longer than in the junction due to the influence of the evolution of the shield at this point. The same behavior is observed at $y = 0.91$, but influenced in a higher degree by the shield temperature evolution.

The comparison of the temperature evolutions in the copper wire case, is analogous. When compared with the constantan results, the initial response of the copper is slightly slower, and the temperature evolutions at the different points closer in terms of the temperature rate evolution. It is explained by the higher conductivity of the copper, that implies higher diffusivity along the wire, and thus smoother temperature gradients between the different positions. Whereas in the constantan case, the effect of the support is little felt close to the junction but greatly affecting the opposite wire extreme.

In the ideal case of no existence of conductive heat between junction and wire, or if equal wire and junction diameters and no conduction flux with the support, the response of the thermocouple would be that of a first order system, Eq. 5. The characteristic would be the time required to complete 63.2 % of its response to a gas temperature step. None of the wire temperature evolutions represented in Fig.7 corresponds to a first order response due to the influence of the support.

Non dimensional junction temperature evolutions are represented in Fig. 8 for the ideal case of adiabatic wire, and constantan wire with two different support conditions: CHT and adiabatic. For each evolution the time to reach 63.2% of the final temperature was used to evaluate the corresponding first order response. When the wires are considered adiabatic, the junction evolution collapses to the first order response. The presence of the wires modifies the temperature response whatever the condition at the support. When no flux occurs between shield and wires the junction reaches the final temperature without the delay caused by the support but it does not correspond to a first order. This result is in agreement with the works of Yule [11] and Petit [5]. The influence of the wires causes an acceleration of the junction response if compared

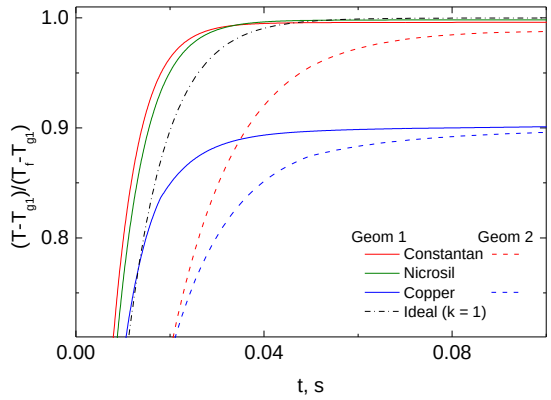

Figure 9: Junction temporal evolution. CHT simulations

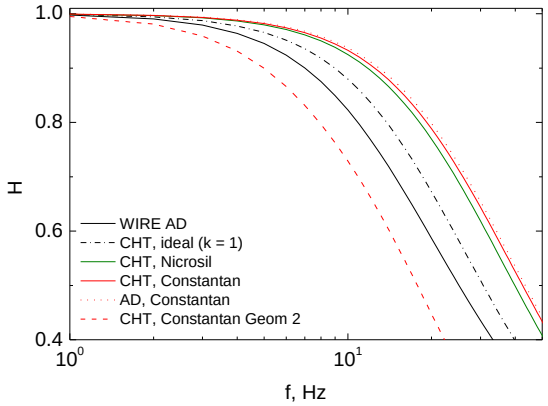

Figure 10: Transfer functions for different wire materials, wire diameter, and support conditions

with the adiabatic wire result. It is instigated by conductive effects from the faster response of a wire element. The evolution at $y = 0.44$ is included in the graph for comparison. A simple decomposition in two first order systems expressing the response of the wire and support as done in cold wires [12] does not accurately reproduce the junction response in the presence of conductive effects.

Figure 9 displays the non dimensional junction temperature evolutions for different wire materials and the two wire diameters (*Geom*1 and *Geom*2). All cases correspond to complete CHT simulations with the consequent possible influence of the slower response of the support. For the cases in which the conductive effects on the junction are not too noticeable ($l/l_c \geq 5$), the higher the wire conductivity the faster the response of a wire element and therefore the faster the response of the junction. Increasing the wire and junction diameters introduces a delay in the response due to the increase of the thermal inertia, and a decrease of the parameter l/l_c, hence an increase of the conductive fluxes.

Assuming the response of a thermocouple can be expressed as linear system model of m-order, the transfer function of the thermocouple in the Z domain can be expressed by the ratio of two m-order polynomials, Eq. 10. A digital procedure [13] was used to determine the invariant transfer function that reproduces better the junction response in each case.

$$H(z) = \frac{b_0 \cdot z^{-d} + b_1 \cdot z^{-1-d} + \ldots + b_m \cdot z^{-m-d}}{1 + a_1 \cdot z^{-1} + a_2 \cdot z^{-2} + \ldots + a_m \cdot z^{-m}} \quad (10)$$

A first order response was found for *Geom*1 with adiabatic wires and for *Geom*3, in accordance with the temporal analyses. A second order system fitted the junction response when the support is adiabatic. A second order system represented likewise the complete CHT simulation in the case of the ideal wire material, where the conductive effects are negligible. For the case of the nicrosil wire, a third order response was found. The higher the effect of the support, the higher the order of the system found to represent the transfer function. The response was found to be that of a 5^{th} order system, for both *Geom*1 and *Geom*2 and constantan wire. For copper wires the response could be considered 5^{th} or 6^{th} order, although the fitting was less accurate. The transfer functions representing the junction responses for several test cases are shown in Fig. 10. The faster response corresponded to constantan wires with cutting frequencies slightly higher than 10 Hz.

7. Conclusions

Gas temperature measurements with thermocouples are to be performed in a transonic flow interacting with finned heat exchangers. Accurate and fast response temperature probes are required.

A new methodology was proposed to numerically resolve temporal evolution of the heat transfer balances within a thermocouple probe. It has been applied to a shielded type thermocouple, providing valuable information of the effect of the design parameters on the different error sources. This procedure overcomes the experimental complexities and inaccuracies providing detailed information of the performances of a given probe in the range of flow conditions of interest.

Results from conjugate heat transfer simulations were analyzed at different values of the main non di-

mensional parameters driving the heat flux within the thermocouple probe. This approach dissects the commonly described experimental "recovery factor" into two steady error sources: flow velocity effects and conductive-convective errors. Radiation effects were shown to be negligible for the flow environment of interest.

Recovery factors for the shielded probe were computed at different Mach and Reynolds numbers. The temperature error increase due to velocity effects is shown, and thus, the benefit of shield designs against bare thermocouples.

Temperature errors due to conduction were analyzed for different wire diameters, wire materials and support temperature conditions. The influence of conductive errors on the junction temperature is mainly dictated by parameter l/l_c, which collects the effects of the wire conductivity, length and diameter and flow convective heat transfer. The decrease of the temperature error with increasing values of l/l_c is reported. If high values of the parameter l/l_c cannot be achieved the conductive temperature error is dominated by the wire support. Results are shown for different support conditions.

Time resolved CHT simulations allowed analyzing the temporal temperature evolution within the probe. The effect of the different heat sources on the response time has been shown. The present numerical approach allowed computing the transfer function of the probe, and analyzing the effects of the temperature errors on the response order.

References

[1] G. E. Glawe, R. Holanda, L. N. Krause, Recovery and Radiation Corrections and Time Constants of Several Sizes of Shielded and Unshielded Thermocouple Probes for Measuring Gas Temperature, Tech. rep., Lewis Research Center, Cleveland, Ohio (1978).

[2] J. Rom, Y. Kronzon, Small shielded thermocouple total temperature probes, Tech. rep., Institute of Technology, Israel (1967).

[3] T. M. Stickney, Recovery and time-response characteristics of six thermocouple probes in subsonic and supersonic flow, NACA TN 3455, Tech. rep., Lewis Flight Propulsion Laboratoty, Cleveland Ohio (1955).

[4] H. I. H. Saravanamuttoo, Recommended practices for measurement of gas path pressures and temperatures for performance assessment of aircraft turbine engines and components, Advisory Report 245, AGARD Advisory Report No. 245 (1990).

[5] C. Petit, P. Gajan, J. C. Lecordier, P. Paranthoen, Frequency response of fine wire thermocouple, J. Phys. E: Sci. Instrum 15 (1982) 760–764.

[6] M. D. Scadron, I. Warshawsky, Experimental determination of time constants and Nusselt numbers for bare wire thermocouples in high velocity air streams and analytic approximation of conduction and radiation errors. NACA TN 2599, Technical Note 2599, Lewis Flight Propulsion LAboratory, Cleveland, Ohio (1952).

[7] C. H. H, A. Kalitinsky, Temperature measurements in high velocity air streams, Trans. ASME 67 (1945) A–25.

[8] F. S. Simmons, Recovery Corrections for Butt Welded stright wire thermocouples in high velocity, high temperature gas streams, Tech. rep., NACA RM-E54G22a (1954).

[9] G. Glawe, F. S. Simmons, T. M. Stickney, Radiation and recovery corrections and time constants of several chromel-alumel thermocouple probes in high temperature high velocity gas streams, Tech. rep., NACA TN-3766 (1956).

[10] R. J. Moffat, Gas temperature measurement.

[11] A. J. Yule, D. S. Taylor, N. A. Chigier, Thermocouple Signal Processing and On-Line Digital Compensation, Journal of Energy 2, No 4 (1978) 223–231.

[12] R. Dnos, C. Sieverding, Assessment of the cold wire resistance thermometer for high speed turbomachinery applications, Journal of Turbomachinery 119, N0 1 (1997) 140–148.

[13] G. Paniagua, R. Dnos, Digital compensation of pressure sensors in the time domain, Experiments in Fluids 32, No 4 (2002) 417–424.

Simulation of a Variable-Combined-Cycle Engine for Dual Subsonic and Supersonic Cruise

Víctor Fernández Villacé

Turbomachinery and Propulsion Department, von Karman Institute for Fluid Dynamics, Belgium, villace@vki.ac.be

Supervisor: Guillermo Paniagua

Associate Professor, Turbomachinery and Propulsion Department, von Karman Institute for Fluid Dynamics, Belgium, paniagua@vki.ac.be.

University Supervisor: José L. Montañés

Professor, Aerothermodynamics and Propulsion Department, Universidad Politécnica de Madrid, joseluis.montanes@upm.es

Abstract

Novel propulsion concepts need to be developed for a feasible sustained high speed flight. To that end, the Scimitar engine benefits from the thermal integration of the cryogenic fuel through a complex combined cycle. This paper presents the numerical model of the Scimitar engine while in air-turbo-rocket configuration, the development of an analysis procedure based on the exergy concept and the engine operational envelope together with its performance figures while flying a determined trajectory between Mach 2.5 and 5.

Keywords: Air-Breathing Engine, Combined Cycle, Exergy, High Speed Propulsion, Numerical Modeling, Variable Cycle.

1. Introduction

The Scimitar engine is a hydrogen-fueled propulsive plant for the aircraft A2, a concept proposed by Reaction Engines Ltd., for the project Long-Term Advanced Propulsion Concepts and Technologies II (LAPCAT II). Scimitar is a variable cycle engine that combines a turbofan-based cycle with an air-turbo-rocket cycle (Fig. 1). The turbofan-based cycle operates from take-off to Mach 2.5. It is augmented with an afterburner (A/B) during the acceleration phase only, having the capability of maintaining a "dry" subsonic cruise regime at Mach 0.9. Between Mach 2.5 and Mach 5 the engine operates as an air-turbo-rocket with a ramjet burner in the bypass. At Mach 5 the vehicle cruises and the cycle is that of a gas generator air-turbo-rocket engine [1]. From take off to Mach 2.5 the core flow is diverted towards the hub turbine (HT) that drives the fan (F); then it is mixed with the air from the by-pass duct. From Mach 2.5 to Mach 5 the core flow is fed into the core main combustion chamber and nozzle and the fan windmills, whose speed is brought down as the by-pass nozzle is progressively closed. In this regime the by-pass acts as a ramjet with an annular exhaust around the core jet.

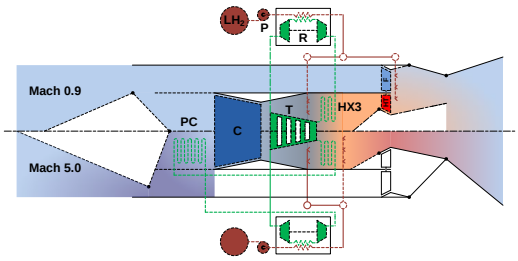

Figure 1: Turbofan (upper half) and air-turbo-rocket (lower half) configurations of Scimitar.

During the supersonic operation, the by-pass nozzle throat is adjusted to provide an optimum matching of the intake and the compressor that minimizes the air spillage. At supersonic cruise regime, the by-pass nozzle is fully closed completing the contour of the core nozzle. The intake has variable geometry: its throat is wide open at low subsonic speeds and closes progressively towards the supersonic regime. Table 1

shows the schedule of each working mode in function of the flight speed: subsonic acceleration, SbA; subsonic cruise, SbC; supersonic acceleration, SpA; supersonic cruise, SpC.

Mach Range	Regime	Mode
0.0 - 0.9	SbA	Turbofan A/B
0.9	SbC	Turbofan
0.9 - 2.5	SpA	Turbofan A/B
2.5 - 5.0	SpA	Ramjet + ATR
5.0	SpC	ATR

Table 1: Variable cycle schedule of Scimitar.

The engine core consists of a compressor that supplies air to the combustion chamber. It is driven by an helium turbine, which is not fluid-dynamically coupled to the compressor as in the conventional turbofan configuration. In this manner the turbine can be constantly operated at high efficiency for the wide operational range of the air compressor. The helium follows a closed Brayton cycle and flows through the precooler (PC) during the supersonic cruise (above Mach 3.1) in order to recuperate the thermal energy of the incoming air. Cryogenic hydrogen acts as heat sink in the loop, which allows the conversion of the recuperated thermal energy into useful work to drive the turbine. The energy interchange between helium and hydrogen is done through a complex recuperator (R) (shown simplified in Fig. 1). The heat exchanger HX3 behind the first injection ramp of the core combustor provides the complementary energy demanded by the helium cycle. Fig. 2 shows the cycle with its corresponding station numbering.

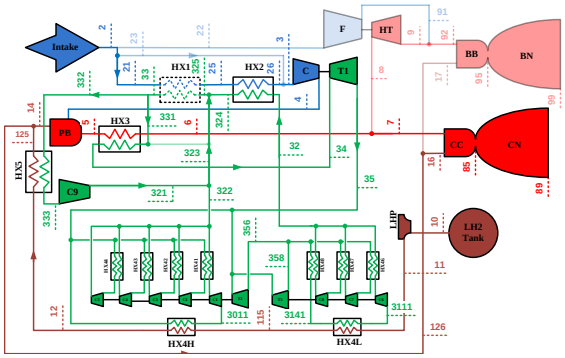

Figure 2: Cycle stations numbering.

During the conceptual design phase of an engine, the numerical model can give an indication about important quantities, e.g. net/gross thrust, specific consumption, specific thrust, which are fundamental when several propulsive concepts are compared. But it is also used to check the proper coupling of the engine modules for off design operations. This is of remarkable importance in the engine Scimitar, which has a novel configuration that combines three different propulsive concepts (turbofan, air-turbo-rocket and ramjet) into the same combined cycle. The proper matching of the major modules: intake, engine core and by-pass duct is to be analyzed to detect penalties on the overall cycle performance at any point of the operational range. The present work explores the performance of Scimitar in the air-turbo-rocket configuration finding its operational limits along the trajectory of the A2 aircraft.

2. Numerical Model

The numerical model is programmed in the symbolic simulation environment EcosimPro by assembling together the engine modules: compressors, turbines, heat exchangers, combustion chambers, nozzles and intake. When available, real geometry and cycle design parameters are used. When they are not, a number of engineering hypotheses are taken to accomplish the design cycle. Finally, the set of differential-algebraic-equations that describe the model behavior is integrated with the differential-algebraic system algorithm DASSL [2].

The model is constructed upon the set of libraries of the European Space Propulsion System Simulation (ESPSS), which integrates the components and functionalities needed for the simulation of propulsive systems. The libraries are being developed under the supervision of the European Space Agency and are intended to become a standard in Europe. Additional ad-hoc elements (heat exchangers and turbomachinery components) have been developed based on and as a complement to the ESPSS set. Here it follows a brief description of the libraries. For a more in dept explanation the reader is encouraged to refer to the user manual [3].

The physical formulation inside each component is time-dependent. The joining elements (manifolds, volumes, valves and junctions) as well as the turbomachinery elements and the intake lack of a spatial discretization. Manifolds and volumes apply the conservation equations, given a characteristic volume, to compute the state variables pressure and enthalpy (p, h). Valve and junction elements make use of their reference cross sectional area to compute the flow variables mass flow and enthalpy flow $(\dot{m}, \dot{H})$ across it ,

accounting for the possible sonic blockage of the section. The dimension of the turbomachinery components is provided indirectly by the scaling factors applied to the characteristic map of a real machine. The ducts in the heat exchangers and the combustors implement the 1D governing equations in their conservative form:

$$\frac{\partial \vec{\omega}}{\partial t} + \frac{\partial \vec{f}(\vec{\omega})}{\partial x} = \vec{\Omega}(\vec{\omega}), \tag{1}$$

where the conservative variables, flux and source terms are respectively:

$$\begin{aligned} \vec{\omega} &= A \left\{ \begin{array}{c} \rho \\ \rho v \\ \rho e \end{array} \right\}; \; \vec{f}(\vec{\omega}) = A \left\{ \begin{array}{c} \rho v \\ \rho v^2 + p \\ \rho v (e + p/\rho) \end{array} \right\}; \\ \vec{\Omega}(\vec{\omega}) &= \left\{ \begin{array}{c} 0 \\ -0.5 \xi \rho v |v| A + p(dA/dx) \\ \dot{q} \end{array} \right\}, \end{aligned} \tag{2}$$

where A is the flow area. The closure relations are provided by the state and calorific equations of the fluid and each expressions for the heat transfer $\dot{q}$ and the friction factor ξ.

The state and calorific description of helium and hydrogen are implemented in ESPSS by a look up routine in the corresponding fluid tables from the NIST database [3]. The hydrogen temperature ranges from 20 K, at the pump exit, to about 1000 K at the preburner inlet and it is considered to be in a normal composition, this is 75% ortho-hydrogen and 25% para-hydrogen, because its properties are available for a wider range (up to 700 K) than for ortho-hydrogen. However, the usage of para-hydrogen would be beneficial for the cycle because of its higher heat absorption capability. In the range $700-1000\ K$ the hydrogen termodynamic behavior can be approximated by that of a semi-perfect gas. Air and the combustion gases inside the combustor components are described as perfect mixtures of semi-perfect gases. The state and calorific relations of the semi-perfect gas are:

$$p = \rho R_g T \tag{3}$$

$$h = h_0 + \int_{T_0}^{T} C_p(T)\, dT, \tag{4}$$

where h_o is the reference for the enthalpy at T_0. The gas exhausting the combustors, flowing into the nozzle or the heat exchanger $HX3$, is characterized as a perfect gas: the specific heats C_p, C_v equal those values computed at the combustor exit and does not vary with the temperature.

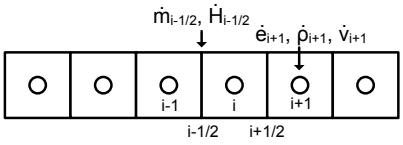

Figure 3: Staggered grid.

The heat addition per unit of length, $\dot{q}$, is computed by means of:

$$\dot{q} = h_c\, \Gamma\, (T_w - T), \tag{5}$$

where Γ is the wet perimeter of the duct under consideration and T_w is the wall temperature. An appropriate correlation for Nusselt number depending on the flow characteristics is used to compute the convective heat transfer coefficient, h_c:

$$h_c = Nu\ k/D_h; \qquad Nu = f(Re, Pr). \tag{6}$$

The friction factor ξ accounts for the pressure loss per unit of length of the duct. It is provided by a correlation valid for laminar, turbulent and transient flows [4]:

$$\xi = k_f\, f/D_h \tag{7}$$

$$f = 8 \cdot \left(\left(\frac{8}{Re} \right)^{12} + (A + B)^{-3/2} \right)^{1/12} \tag{8}$$

$$A = \left(2.457 \cdot ln \frac{1}{(7/Re)^{0.9} + 0.27 \cdot \epsilon/D_h} \right)^{16} \tag{9}$$

$$B = (37530/Re)^{16} \tag{10}$$

The correction coefficient k_f serves to adjust the pressure loss along the fluid vein to the required design value.

Eq. 1 is solved with a centered scheme in a staggered mesh, where the state variables (e_i, ρ_i, v_i) are computed at the cell nodes and the fluxes $(\dot{m}_i, \dot{H}_i)$ at the cell interfaces, Fig. 3.

2.1. Combustion chambers and nozzles

During the combustion process the composition of the combustion gases is an additional dependent variable. Under the hypothesis of chemical equilibrium, the equilibrium composition is that one which minimizes the Gibbs energy for the current state (p, T) of the mixture. For each of the grid nodes, at each time step, the minimization problem is solved in an iterative manner together with the conservation Eqs. 1.

Along the nozzle following the combustor, the flow is supposed to be frozen, the compositions being the

same as calculated in the outlet cell of the combustor. Despite that the software offers the capability of computing the equilibrium composition of the flow, this calculation was discarded to speed up the simulations. Also with this same purpose, a one- and two-nodes spatial discretizations were chosen respectively for the preburner and the main combustor chamber. For the combustion of air with hydrogen, 19 reacting species, with the elements H, N, O, are considered in the equilibrium calculation. The geometry is characterized by the distribution of cross-sectional area along the axis, $A(x)$, in (Eq. 2).

Some of the heat generated in combustor is transfered to the fuel and the oxidizer in their respective manifolds. But, apart from this, the preburner surface is supposed to be adiabatic. However, the nozzle is cooled by radiation to the environment, whose temperature varies along the vehicle trajectory accordingly to the International Standard Atmosphere (ISA) model. A uniform view factor of one is considered on the external surface of the nozzle to compute the radiated heat as predicted by the law of Stefan-Boltzmann. For the heat transfer on the internal surface of the nozzle, the convective heat transfer coefficient h_c is computed from the correlation of Bartz [5] and the law of Stefan-Boltzmann for the radiated heat. The heat flux from the fluid inside each cell is then:

$$\dot{q}_{wall\ i} = h_{c\ i}\,\Gamma_{wall\ i}\,(T_{wall\ i} - T_{a\ i}) \quad (11)$$

$$+ \sigma\,A_{wall\ i}\,(T^4_{wall\ i} - T^4_i), \quad (12)$$

where $\Gamma_{wall\ i}$ is the wet perimeter of the i^{th} cell, with bulk and solid wall temperatures of T_i and $T_{wall\ i}$, σ is the Stefan-Boltzmann constant. The adiabatic wall temperature $T_{a\ i}$ is approximated by:

$$T_{a\ i} = T_i\,(1 + Pr_i^{0.33}\,(\gamma_i - 1)\,0.5\,M_i^2), \quad (13)$$

being Pr_i, M_i and γ_i the Prandtl and Mach numbers and the ratio of specific heats in the i^{th}-cell. The correlation of Bartz provides the expression of the film coefficient:

$$h_c = 0.026\,\mu_i^{0.2}\,(k/\mu)_i^{0.6}\,Cp_i^{0.4}\cdot \quad (14)$$

$$\cdot\ \dot{m}_{th}^{0.8}/A_i^{0.9}\,(0.25\,\pi\,D_{th}/R_c)^{0.1}, \quad (15)$$

where $\dot{m}_{th}$, D_{th} and R_c are respectively the throat mass flow, diameter and curvature radius; k_i, μ_i and Cp_i are the thermal conductivity, viscosity and specific heat at constant pressure of the combustion gases at the grid position i and A_i is the cross area of the section i. In the equations above, the temperature dependent gas properties (Pr_i, k_i, μ_i and Cp_i) are evaluated at a temperature in between the bulk and the wall temperatures.

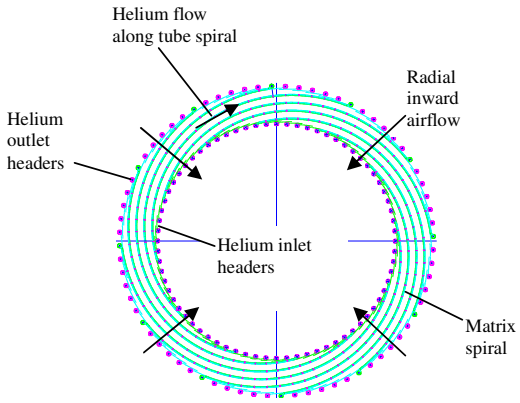

Figure 4: Frontal view of one precooler module showing the spiral of tubes [6].

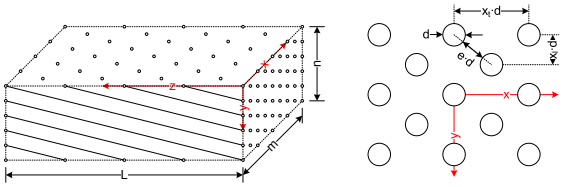

Figure 5: Equivalent matrix of tubes in cross-flow.

The flow in the nozzle is solved from Eq. 1-2 disregarding the unsteady and viscous (ξ) terms. A 5-node discretization is taken.

2.2. *Heat exchangers*

Three different models of heat exchanger were developed to simulate the Scimitar precooler (HX1 and HX2), reheater (HX3) and the regenerator modules (HX4L, HX4H, HX5, and the He-He regenerators). They are based on the existing capabilities of the ESPSS libraries. The fluid flow is computed as described in the above paragraphs, being only the geometry and heat transfer behavior characteristic to each one of them.

2.2.1. *Precooler*

The precooler contains two modules consisting of a number of tubes with $d = 0.96$ mm external diameter tangentially mounted in a spiral around the engine axis. The air flows radially inwards across the tubes and the helium inside the tubes follows the spiral path from the internal to the external headers, Fig. 4. The

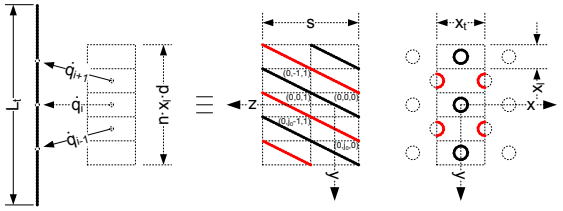

Figure 6: Equivalent computational domain of the periodic flow field. The perimeter of the section Γ in Eq. 5 is equal in every cell of the staggered arrangement (bold contours in the rightmost figure).

low temperature module HX2 is placed coaxially inside the high temperature module HX1, both sharing a common manifold. Because the ratio of the module diameter to the tube size is in the order of 10^3, the curvature effect on the flow field can be discarded. The planar equivalent bank of staggered tubes in crossflow is shown in Fig. 5. The transversal and longitudinal pitches are respectively of 2 and 1.5 tube diameters (x_t, x_l), which results in a passage minimum width of 0.8 tube diameters.

Under the assumption of uniform boundary conditions at the matrix inlet and outlet surfaces the flow is periodic. The dimensions of the periodic domain in the transversal plane XZ are $x_l \times s/2$, being s the tangential tube pitch, Fig. 6. The thermal field in the domain along the Y-direction through the cell $(i, j, k) = (0, 0, 0)$ is T_{0j0} with $j = 1, n$ and i, j, k the indexes in x-, y-, z-directions respectively and n the number of nodes. The temperature distribution seen by the helium pipe passing through this cell is T_{0jk}, with $j = 1, n$ and $k = -j$. Because the temperature field is periodic in z-direction: $T_{ijk} = T_{ij0}$, $\forall j = 1, n$, the helium pipe through $(0, 0, 0)$ sees the same temperatures as those along the periodic domain. In consequence, the flow is solved by applying the 1D conservation equations Eq. 1 to a single helium pipe and to the periodic domain, having both the same nodal temperatures in a counter flow disposition. The heat capacity of the tube wall is also taken into account by the balance of heat fluxes in the wall:

$$\dot{q}_{air\ j} + \dot{q}_{hel\ n-j} = -\frac{(m \cdot C)_{wall}}{n} \cdot \dot{T}_{wall\ n-j} \qquad (16)$$

$$j = 1, n \qquad (17)$$

being $(m \cdot C)_{wall}$ the heat capacity of the wall of one single pipe.

The mass flow and heat flux through the overall matrix equal the contribution of one single domain times the total number of tubes in the matrix. The number of discretization nodes is $n = 20$, equally spaced. The helium pipe has the same internal diameter and length as the tubes of the real module. The air duct cross sectional area is smaller than that of the periodic domain and equals the passage minimum area of the matrix:

$$\frac{A_{min}}{A} = \frac{2 \cdot e \cdot d \cdot L}{x_t \cdot d \cdot L} \qquad (18)$$

$$= \frac{2}{x_t}\left(\sqrt{x_t^2/4 + x_l^2} - 1\right) \approx 0.803, \qquad (19)$$

being A the surface of matrix perpendicular to the flow.

The distributed pressure loss in both the helium and air sides is computed from Eq. 10, with some adjustment of the correction coefficient k_f to match the module design pressure loss.

The length of the interface helium-air for the calculation of the heat flux, Γ in Eq. 5, is the pipe external perimeter. The Nusselt number on the helium side is computed with the following extension of the Dittus-Boelter correlation [3], valid from laminar through transitional to turbulent regimes:

$$Nu = (Nu_{lam}{}^{16} + Nu_{tur}{}^{16})^{1/16} \qquad (20)$$

$$Nu_{tur} = 0.023 \cdot Re^{0.8} \cdot Pr^{0.4} \qquad (21)$$

$$Nu_{lam} = 4, \qquad (22)$$

with the Reynolds number based on the hydraulic diameter D_h.

With respect to the heat transfer on the air side, Fig. 7(a) summarizes the survey carried out on previous works on heat transfer through a bank of staggered tubes in crossflow. The results shown are for the heat transfer in a square bank ($x_t = x_l = 2$) under the hypothesis of isothermal boundary condition. The analytical correlation of Khan for steady flow is close to the empirical results by Hausen. The steady quasi-3D numerical calculations of Nakayama where obtained over a bank of square tubes. The results for the unsteady fully developed flow calculations by Beale show that the staggered configuration is naturally unstable without any external excitation, hence the averaged Nusselt number is nearly the same in both cases: with and without the external stimulus. Finally it is the expression provided by Khan [7] the one used in the present application for being conservative respect to the numerical results and because it retains the influence of the matrix geometry in an analytical expression:

$$Nu = C \cdot Re^{1/2} Pr^{1/3} \qquad (23)$$

$$C = \frac{0.61 x_t{}^{0.091} x_l{}^{0.053}}{1 - 2 \cdot exp(-1.09 x_l)}, \qquad (24)$$

where the Reynolds number is based on the average speed in the passage minimum area and the external diameter of the tube.

Fig. 7(b) compares the values of Nusselt number by Khan and Hausen for the geometry and operational range ($Re \approx 300-600$) of the Scimitar precooler. The analytical expression of Khan for a single row of tubes in cross flow (blockage ratio $b = 0.55$) shows values very close to those of Hausen.

2.2.2. *Reheater*

The reheater (HX3) is located downstream of the preburner (PB) with the purpose of maintaining a constant inlet temperature to the helium turbine (T1) during any flight condition. It is composed by an inner and outer cylindrical shrouds with a number of plates N_p radially disposed between them. The gas from the preburner flows along the axis whereas the helium does it radially inward, from the outer to the inner shroud and through the plates, Fig. 8(a). The ratio of the passage span to its mean diameter is 2:5 but because the passage slenderness is very high (1:120) the curvature of the inner/outer shroud is deprecated and the passage assumed to be rectangular. Each plate is divided into a number n_z of strips, each one having a number N_t of square channels with a cross section of 1.5 x 1.5 mm^2. The helium streams flow along these channels in the direction of $r < 0$ and the gas flows along the direction $z > 0$ between the plates. The tangential pitch s_i is the one measured at the inner shroud in the real reheater, minor (hence critical) than the one at the outer shroud, Fig. 8(b).

Under the hypothesis of uniform boundary conditions on the gas inlet and outlet planes, only one fluid passage is discretized, being the total flow and heat flux N_p times that of a single passage. With the same assumption done for the helium, only one plate is representative of the whole reheater. The flow in the helium channels is solved with a pseudo-2D discretization of the plate in the *RZ*-plane: the flow inside each channel of the same strip is solved with a 1D discretization along the r-direction and n_z strips are considered along the z-direction. The thermal connectivities between the $n_z + 1$ fluid veins are established assuming that the wall temperature along the strip is constant and equal to the gas bulk temperature for each axial position: $T_{wall\ i,k} = T_{gas\ k}$ with $i = 1, n_r$ and $k = 1, n_z$, Fig. 8(c). The thermal capacity of the wall is taken into account when applying the energy

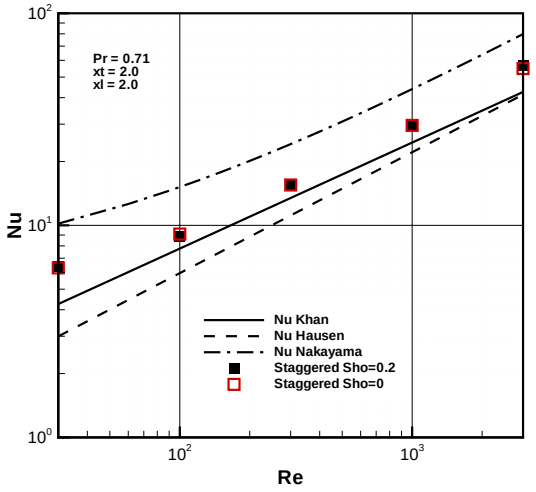

(a)

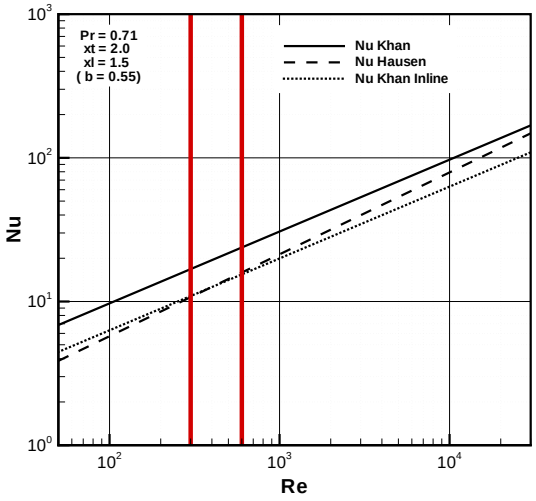

(b)

Figure 7: (a) Comparison of the Nusselt predictions by Hausen [8], Khan [7], Nakayama [9] and Beale [10] for the staggered square tube bank. The calculations of Beale were done with ($Sh_o = 0.2$) and without ($Sh_o = 0$) initial perturbation. (b) Comparison of the Nu predictions on the geometry of the precooler by Khan (Eq. 24) and Hausen [8]. The results of Khan for the single row in crossflow (Khan inline) [11] are shown as well. Scimitar operational range is shown between the red lines.

balance to the wall:

$$\dot{q}_{gas\ k} + \sum_{i=1}^{n_r} \dot{q}_{hel\ ik} = -(m \cdot C)_{wall} \cdot \dot{T}_{wall\ k} \qquad (25)$$

$$k = 1, n_z \qquad (26)$$

being $(m \cdot C)_{wall}$ the heat capacity of the wall of a single strip.

A discretization in $n_r = 5$ and $n_z = 10$ nodes is used respectively for the helium and gas flows. In the calculation of the heat flux into the helium and the combustion gas $\dot{q}$, in Eq. 5, the convective heat transfer coefficient is computed using the previous Eqs. 20-22, in which the Reynolds number is based on the hydraulic diameter:

$$D_h = 2s_i(D_o - D_i)/(2s_i + D_o - D_i). \qquad (27)$$

2.2.3. *Regenerator*

The regenerator comprises two types of units: helium-to-helium (HX41-44 and HX46-48) and helium-to-hydrogen (HX4H, HX4L and HX5), both of them are modeled as alternatively stacked layers of heating and cooling channels characteristic of the compact plate / channel micro heat exchangers [12]. Each unit contains a number M of modules circumferentially disposed around the engine axis. As in the previous cases, curvature effects can be disregarded as the ratio of the channel height to its radial position from the engine centerline is in the order of 10^{-4}. Each module has N rows of respectively M_h and M_c heating and coolant channels each being, the total number of channels per regenerator M x N x M_h x M_c. The channels are embedded in the same base material and the rows are disposed in counterflow, Fig. 9. The purpose of this geometry is twofold: firstly laminar regime can be achieved along the full length of the channels which minimizes the pressure drop. Secondly the cooling performance is significantly improved by the large increase of the heat exchange area, in the order of 10^4 m^2 per unit. Both heating and coolant channels have a cross section of 50 x 50 μm^2 and are count in a number of $\approx$ 10^7 per module, hence the 1D fluid field along any two hot and cold channels is representative of the overall module.

The energy equation applied to the wall is the same Eq. 17, for which now the air and helium flows refer to the heating and coolant channels respectively and $(m \cdot C)_{wall}$ is the thermal capacity of the complete matrix, the number of nodes being $n = 30$. The convective heat transfer coefficient in Eq. 5 is obtained by

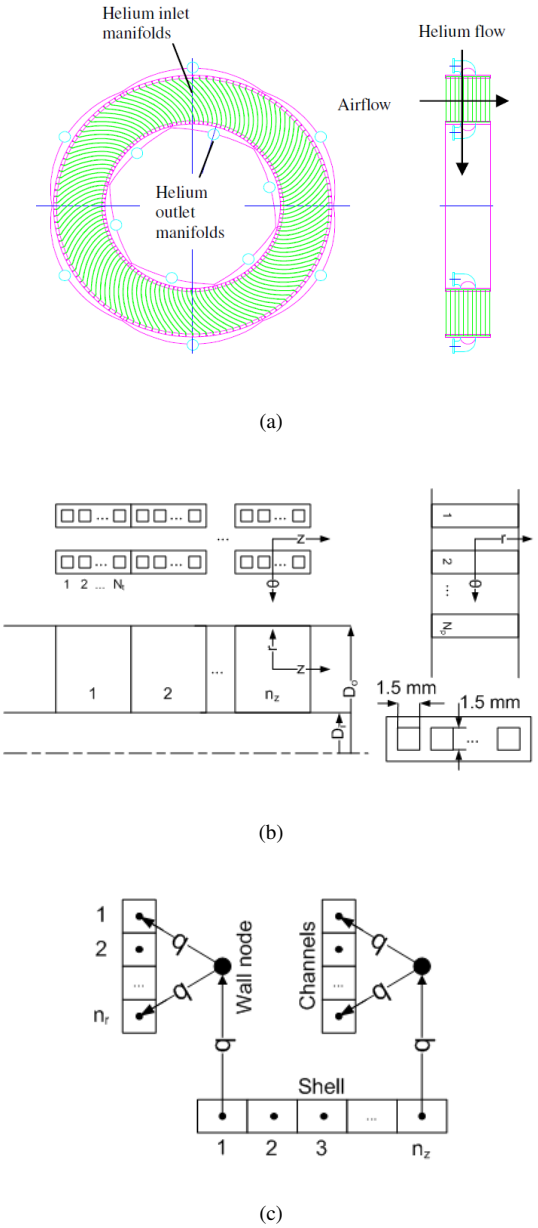

Figure 8: Reheater module: (a) frontal and side view [6], (b) geometrical definition of the numerical model and (c) thermal connectivities between gas and helium channels.

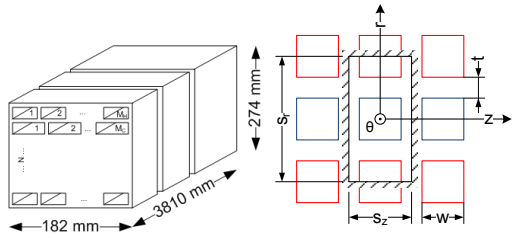

Figure 9: Geometry of the regenerator modules.

assuming a constant Nusselt number of 10 along the channels for both hot and cold streams.

2.3. Turbomachinery

They make use of steady experimental characteristics to predict the machine off-design performance in terms of its pressure ratio π, mass flow rate $\dot{m}$ and adiabatic efficiency η. The characteristic maps are given as functions of the corrected speed $\tilde{N}$ and the β-parameter:

$$\pi(\tilde{N},\beta)\,; \qquad \tilde{\dot{m}}(\tilde{N},\beta)\,; \qquad \eta(\tilde{N},\beta) \tag{28}$$

$$\tilde{N} = \frac{\Omega/N_d}{\sqrt{\theta}} \cdot \frac{30}{\pi_n} \tag{29}$$

$$\tilde{\dot{m}} = \dot{m} \cdot \sqrt{\theta_{in}}/\delta_{in} \tag{30}$$

In order to fulfill the performance at the design point, the turbomachine is resized applying constant factors to the characteristic map $(\Pi, \tilde{M}, H)$ of a known machine:

$$\pi = 1 + K_\pi \cdot (\Pi(\tilde{N},\beta) - 1) \tag{31}$$

$$\tilde{\dot{m}} = K_{\dot{m}} \cdot \tilde{M}(\tilde{N},\beta) \tag{32}$$

$$\eta = K_\eta \cdot H(\tilde{N},\beta) \tag{33}$$

The map of the helium turbine (T1) was computed from a CFD off-design analysis [13] of the counter rotating machine designed for Scimitar during the previous project LAPCAT I [14].

The maps of the air compressor and the other units in the regenerator are selected from the map database elaborated by Kurzke [15]. The compression stages of the regenerator are supposed to perform like a single stage mixed flow compressor, whose characteristics [16] are rescaled for each unit (C1-C8). The turbines T2 and T3 are based on the characteristics of the first stage of a highly loaded axial turbine [17]. In these helium machines, the correction for the working fluid is done by means of the parameter θ in Eqs. 29, 30:

$$\theta = R_{hel} T_{in}/(RT_{in})_{std}, \tag{34}$$

with R_{hel} the gas constant of the helium and in the denominator, the gas constant of the air and the standard total inlet temperature for which the map was obtained. The map of the air compressor corresponds to that of an axial high pressure core compressor [18].

The task of the helium recirculator (C9) is to increase the cooling through the precooler while flying at high speed for a short range of Mach numbers. Because it only overcomes the pressure loss through the high temperature module (HX1) and the regenerator (HX5), its consumption is very low ($\approx$ 100 kW) in comparison with the compression stages, which is ten times larger. Consequently its power is not accounted for in the engine evaluations. Moreover it is supposed to work continuously at an efficiency $\eta = 0.9$, no matter the mass flow or pressure ratio. This simplifies the engine model and accelerates the calculations. The liquid hydrogen pump (LHP), whose power is of the same order as that of the recirculator, is not included in the model for the same reason.

The energy balance yields that the mechanical power in the shaft equals the power to the fluid side:

$$P = \dot{m} \cdot \Delta h_t \tag{35}$$

$$P = T \cdot \Omega \tag{36}$$

$$\frac{\Delta h_{t,s}(p_{t_{in}}, T_{t_{in}}, p_{t_{out}})}{\Delta h_t} = \begin{cases} \eta; & (turb.) \\ 1/\eta; & (comp.) \end{cases} \tag{37}$$

In Eq. 37, $\Delta h_{t,s}$ is the total enthalpy change of an isentropic evolution from inlet to outlet status.

The excess of torque $T_{sh} - T$ accelerates the rotor, with inertia I:

$$T_s(\Omega; t) - T = I \cdot \dot{\Omega}, \tag{38}$$

This equation relaxes the mechanical constraint by allowing a difference between the torque applied on the shaft T_{sh} and the torque that the rotor transfers to the fluid T. In a similar way the constraint on the machine discharge duct is relaxed:

$$\dot{m} - \dot{m}' = \tau \cdot \ddot{m}', \tag{39}$$

being $\dot{m}$ the flow rate read from the map, $\dot{m}'$ the actual flow rate passing through the machine and $\ddot{m}'$ its time derivative. The time τ is a measure of the convective characteristic time in the duct of the turbomachine:

$$\tau \approx \frac{l_{c_{in}} + l_{c_{out}}}{2 \cdot a_{in}}, \tag{40}$$

where $l_{c_{in/out}}$ is the characteristic length of the inlet/outlet ducts and a_{in} the speed of sound computed

at the inlet of the machine. The solution of this differential equation must satisfy the constraint imposed by the discharge duct:

$$\dot{m}'(\dot{m}, \tau, t) = f(\pi; t), \tag{41}$$

where f is the characteristic of the discharge duct.

The combination of Eq. 28-38 establishes the form of the mechanical constraint on the operating point, $I_\Omega \equiv 0$; whereas Eq. 28, 30-32, 39 and 41 determine the constrain imposed by the discharge duct, $I_{\dot{m}} \equiv 0$. The solution of the system of equations:

$$\begin{cases} I_\Omega(\tilde{N}, \beta; K_\pi, K_{\dot{m}}, K_\eta, N_d, T_s, \vec{B}, \vec{P}; t) = 0 \\ I_{\dot{m}}(\tilde{N}, \beta; K_\pi, K_{\dot{m}}, f, \vec{B}, \tau; t) = 0 \end{cases} \tag{42}$$

$$\vec{B} = (\delta_{in}, \theta_{in}); \ \vec{P} = (\Omega_0, I) \tag{43}$$

is the transient operating line of the turbomachine $\tilde{N}(t), \beta(t)$ which, for a given machine size $\{K\}_{\pi,\dot{m},\eta}, N_d$, is determined by the inlet conditions $\vec{B}$, the discharge characteristic f and the mechanical constraint T_s. The integration constant Ω_0 is the initial shaft speed.If $\dot{\Omega} = \dot{m}_{out} = 0$, the previous system for the steady operating line is:

$$\begin{cases} I_{\Omega_0}(\tilde{N}_0, \beta_0; K_\pi, K_{\dot{m}}, \vec{B}, T_s \cdot N_d, \eta_0 \quad) = 0 \\ I_{\dot{m}_0}(\tilde{N}_0, \beta_0; K_\pi, K_{\dot{m}}, \vec{B}, f \qquad\qquad\quad) = 0 \end{cases} \tag{44}$$

Normally the turbomachine is linked to other fluid components like pipes, manifolds or heat exchangers and mounted on the same spool than other $m-1$ machines. The steady state of this assembly cannot be known a priori. However the stagnation pressures and temperatures in the fluid components can be approximated by those of the design cycle. These provide the inlet conditions $\vec{B}$ and the value f. The speed N_d, operating point $(\tilde{N}_0, \beta_0)$ and efficiency η_0 are design values. The size of the machines is then determined by m equations like Eq. 44 and the closure equation introduced by the common spool: $\sum_{i=1}^{m} T_{s_i} = 0$. Fig. 10 shows the input data and design values required for the matching of a compressor with a turbine on the same shaft.

3. Results

The performance of Scimitar in the air-turbo-rocket configuration is evaluated in the Mach range from Mach 2.5 to supersonic cruise at Mach 5. Understanding the behavior of this configuration is crucial as it constitutes the propulsive core of the engine, being the

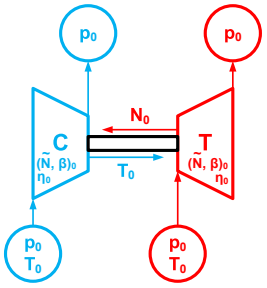

Figure 10: Input data to size the compressor-turbine matching.

turbofan and ramjet configurations subtle variations of it.

Exergy is the potential work that can be extracted from a system that interacts with the environment in a reversible manner. It is a measure of the quality of the energy contained by a system or transfered by a process in relation with the environment. It will serve to establish a common definition of the efficiency that can be applied without distinction to the overall engine as to its subcomponents.

The combination of the First and the Second Principle of Thermodynamics yields the expression of the exergy balance [19] in a control volume (CV):

$$\dot{E}_{CV} = (1 - T_0/T)\dot{Q}_T + \dot{W} + \tag{45}$$

$$+ \sum_i (\dot{m}\epsilon)_i - \sum_o (\dot{m}\epsilon)_o - \dot{I}, \tag{46}$$

where $\dot{E}_{CV}$ is the unsteady accumulation of exergy in the control volume and the terms in the right hand side account respectively for the availability transfer due to heat, work and mass exchange through the boundaries. The last term is the exergy destruction or irreversibility associated to the process taking place in the control volume. It is proportional to the entropy production $(\dot{\sigma}_p)$ and the environmental temperature (T_o) through the Gouy-Stodola theorem: $\dot{I} = T_o \dot{\sigma}_p$. The procedure to evaluate the specific exergy ϵ of the incoming (i) and outgoing (o) fluid streams is explained in Annex A. The specific exergy at each engine station is shown in Table 2. They are evaluated from the standard reference environment at $T_o = 288.15\ K$, $p_o = 1\ atm$ and relative humidity $\phi_o = 46\ \%$, which corresponds to a molar content of $7750 ppm$ of water in dry air at standard conditions [20].

Table 2 also shows the pressures, temperatures and mass flow rates corresponding to different stations of the Scimitar engine during cruise at Mach 5 and 25 km altitude. In this condition the by-pass duct is closed, hence the fan (F), hub turbine (HT), by-pass burner

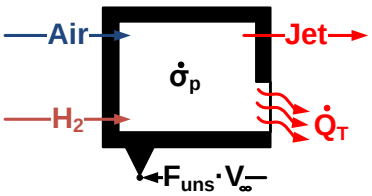

Figure 11: Control volume used in the effectiveness calculation.

(BB) and nozzle (BN) are not in operation (shadowed components in Fig. 2). The corresponding station numbering is shown in Fig. 2.

Applying Eq. 46 to the control volume in Fig. 11, which represents the engine, and considering stationary regime yields:

$$\underbrace{F_u\, v_\infty}_{\dot{W}_u} = \underbrace{(\dot{m}\epsilon)_{air} + (\dot{m}\epsilon)_{H_2}}_{\dot{W}_a} - \tag{47}$$

$$\underbrace{-T_0\dot{\sigma}_p + (1 - T_0/T)\dot{Q}_T - (\dot{m}\epsilon)_{jet}}_{-\dot{I}}, \tag{48}$$

where $\dot{W}_u$ is the useful propulsive power of the uninstalled thrust F_u at the flight speed V_∞ and $\dot{W}_a$ is the available power computed from the exergy inflow of air (station 0) and hydrogen (station 11). The rightmost term $\dot{I}$ is the irreversibility incurred by the system, composed by the internal energy waste, the heat released across the non adiabatic boundaries and the exergy lost with the exhaust jet (station 89). The non-adiabatic boundary is the nozzle wall, which is cooled by radiation to the ambient. The exergy lost with the jet is the inherent cost of generating thrust in the reaction engine. The uninstalled thrust is computed as:

$$F_u = \dot{m}_{jet} v_{jet} - \dot{m}_{air} v_\infty + (p_e - p_{atm}) A_e, \tag{49}$$

with v_∞ the flight speed, p_e and A_e the static pressure and cross area at the nozzle exit section and p_{atm} the atmospheric pressure at the given flight altitude. Based on the exergy balance of Eq. 48 a "second-law efficiency" or effectiveness can be defined as the ratio of useful to available power:

$$\eta_\epsilon = \frac{\dot{W}_u}{\dot{W}_a} = 1 - \frac{\dot{I}}{\dot{W}_a} = 34.3\% \tag{50}$$

Taken as a reference, the effectiveness computed by Etele for a turbojet cruising at Mach 0.8 ranged from 15% to 17.5% [21]. Scimitar doubles this effectiveness thanks to the thermal integration of the fuel in the cycle showing its enormous potential for very high speed fight.

The engine is a system with two degrees of freedom. The first one is the pair of values for the stagnation inlet temperature and pressure of the air, which are determined for the given ascent trajectory of the vehicle. The second is the fuel inflow or engine throttle, which directly acts on the engine thrust. Additional four engine variables are governed by control laws that set the engine off-design performance during throttling and acceleration towards supersonic cruise. They are the helium turbine inlet temperature, the air flow rates across both bypasses of the precooler modules and the helium flow in the recirculator loop.

Fig. 12 shows the regulation of the engine mass flows by these control laws while the engine accelerates from Mach 2.5 to Mach 5 for a constant mixture ratio of 43. The inlet temperature of the helium turbine is maintained at a constant value of $1000K$ by diverting fuel from the main combustion chamber (CC) towards the preburner (PB). The engine designer establish $635K$ as the maximum inlet temperature of the air compressor [1]. To fulfill this requirement the air from the intake starts flowing through the precooler (PC) at Mach 3 as the bypass (BP PC) closes gradually. The precooler reaches full operation above Mach 3.5. With respect to the regulation of the precooler temperatures, at Mach numbers less than 3.8, only the second precooler module (HX2) is needed to cool down the incoming air and the first module (HX1) is bypassed. Above Mach 4.8 the circulator (C9) and the additional regenerator module (HX5) increase progressively the flow of cool helium through the first precooler module (HX1) in order to maintain its temperature below $1000K$.

Fig. 13 shows the operational envelope of the Scimitar core. The flight Mach number and altitude are related through the A2 vehicle trajectory. The uninstalled thrust, effectiveness and specific thrust (defined as the ratio of uninstalled thrust to fuel mass flow) at each flight condition and fuel inflow values are shown. The domain of operating points is bounded by the turbomachinery operational limits, set by their respective characteristic maps as the maximum / minimum allowed values of the parameter β and the corrected speed.

4. Conclusions

Based on the existing capabilities of the European Space Propulsion System Simulation, appropriate models of the heat exchanger modules and the turbomachinery elements have been developed to better represent their physical behavior and therefore the

	Design point at Mach 5			
Station	$P\ [bar]$	$T\ [K]$	$\dot{m}\ [kg\ s^{-}]$	$\epsilon\ [kJ\ kg^{-}]$
0	14.1	1247	176.5	862
2	3.4	1247	176.5	744
25	3.1	853	176.5	416
3	2.8	633	176.5	255
4	12.1	971	176.5	612
11	18.0	20	4.05	129993
115	17.7	289	4.05	121872
12	16.7	832	4.05	125276
125	14.3	978	4.05	126569
14	14.3	978	0.04	126569
16	14.3	978	4.01	126569
5	10.3	995	176.5	642
6	10.2	997	176.5	643
CC	9.0	2615	180.6	-
PB	10.4	993	176.5	-
89	0.02	704	180.6	3569
3011	128.7	302	11.1	2940
3111	47.3	32	11.1	4351
3141	47.6	295	11.1	2317
32	199.1	587	33.3	3753
321	198.2	849	10.0	4507
322	198.2	849	55.1	4507
323	198.2	849	65.1	4507
324	198.1	842	33.3	4483
33	197.2	1001	97.4	5046
34	196.6	1000	88.4	5039
35	129.2	859	88.4	4269
356	48.4	596	22.2	2839
358	48.4	614	11.1	2856

Table 2: Cruise cycle at Mach 5. The corresponding stations can be seen in Fig. 2. The values of pressure and temperature are for stagnation conditions except for *CC*, *PB* and 89, which refer respectively to the values inside the combustion chamber, preburner and nozzle exit section.

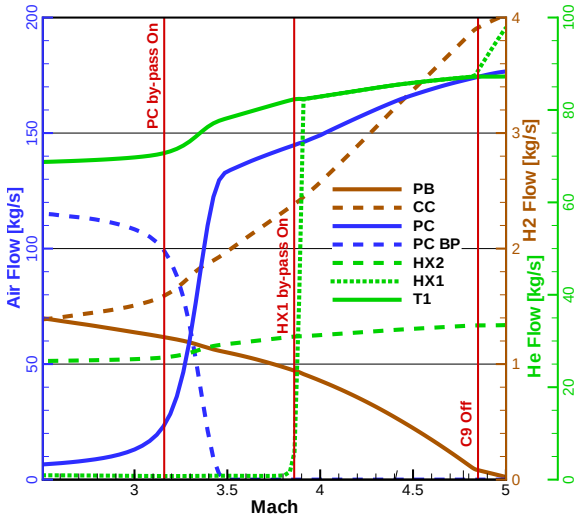

Figure 12: Engine mass flow rates during acceleration from Mach 2.5 to cruise at Mach 5 at a constant mixture ratio of 43.

model accuracy. The simulation of Scimitar in its air-turbo-rocket configuration provides the foreseen performance during supersonic cruise and that of the engine core during acceleration from Mach 2.5 to Mach 5 as well as its operational envelope. The dynamic nature of the model allows the introduction of control laws in a natural way.

Finally, the exergetic analysis provides a meaningful definition of the efficiency or effectiveness of the system, which is an indication of the engine degree of thermal integration within its environment. A crucial issue for high speed propulsion.

Acknowledgments

This work was performed within the Long-Term Advanced Propulsion Concepts and Technologies II project investigating high-speed air-breathing propulsion. LAPCAT II, coordinated by ESA-ESTEC, is supported by the EU within the 7th Framework Programme, Transport, Contract no.:ACP7-GA-2008-21 1485.

References

[1] F. Jivraj, R. Varvill, A. Bond, G. Paniagua, The scimitar precooled mach 5 engine, in: 2nd European Conference for Aerospace Sciences, EUCASS, Brussels, Belgium, 2007.

[2] L. R. Petzold, DASSL: Differential Algebraic System Solver, Tech. rep., Sandia National Laboratories, Livermore, California (1983.).

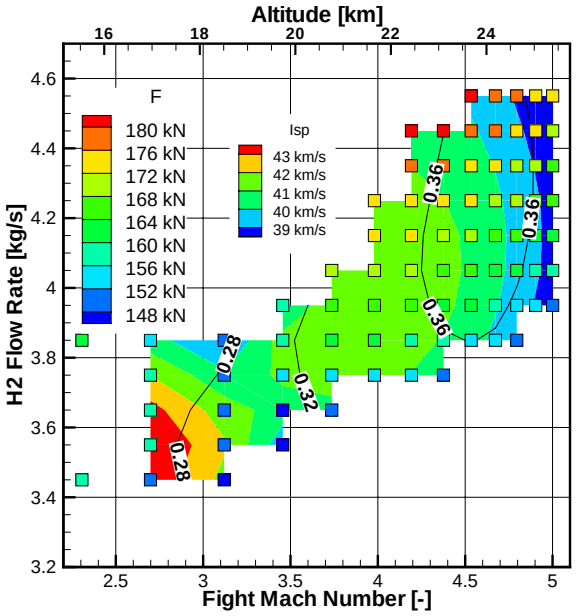

Figure 13: Scimitar core operational envelope. The filling color of each square indicates uninstalled thrust , the colored contours indicate the specific impulse and the effectiveness is shown by the contour lines.

[3] ESA, Astrium-Bremen, Cenaero, Empresarios Agrupados Int. and Kopoos, ESPSS EcosimPro Libraries User Manual, Tech. Rep. TN-4140, European Space Agency, version 2.0 (May 2010).

[4] S. W. Churchill, Friction-factor equation spans all fluid-flow regimes, Chemical Engineering 84 (24) (1977) 91–92.

[5] D. R. Bartz, Turbulent boundary-layer heat transfer from rapidly accelerating flow of rocket combustion gases and of heated air, Advances in Heat Transfer 2 (1965) 1–108.

[6] R. Varvill, Heat exchanger development at reaction engines ltd, in: 59th International Astronautical Congress, IAC-08-C4.5.2, International Astronautical Federation, IAC, Glasgow, Scotland, 2008.

[7] W. A. Khan, J. R. Culham, M. M. Yovanovich, Convection heat transfer from tube banks in crossflow: Analytical approach, International Journal of Heat and Mass Transfer 49 (2006) 4831–4838.

[8] H. Hausen, Heat Transfer in Counterflow, Parallel Flow and Cross Flow, McGrawHill, New York, 1983.

[9] A. Nakayama, F. Kuwahara, T. Hayashi, Numerical modelling for three-dimensional heat and fluid flow through a bank of cylinders in yaw, Journal of Fluid Mechanics 498 (2004) 139–159.

[10] S. B. Beale, D. B. Spalding, A numerical study of unsteady fluid flow in in-line and staggered tube banks, Journal of Fluids and Structures 13 (1999) 723–754.

[11] W. A. Khan, J. R. Culham, M. M. Yovanovich, Fluid flow and heat transfer from a cylinder between parallel planes, Journal of Thermophysics and Heat Transfer 18 (2004) 395–403.

[12] H. Webber, S. Feast, A. Bond, Heat exchanger design in combined cycle engines, in: 59th International Astronautical Congress, IAC-08-C4.5.1, International Astronautical Federation, IAC, Glasgow, Scotland, 2008.

[13] R. Bontempo, Performance analysis of a contrarotating turbine, Stagiaire Report VKI SR 2010-11, Von Karman Institute for Fluid Dynamics (June 2010).

[14] G. Paniagua, S. Szokol, H. Kato, G. Manzini, Contrarotating turbine aerodesign for an advanced hypersonic propulsion system, Journal of Propulsion and Power 24 (6) (2008) 1269–1277.

[15] J. Kurzke, Component map collection 2 (2004).

[16] Tech. Rep. 21-4460-2.3, Air Force Mixed-Flow Compressor Garrett Turbine Engine Company (1982).

[17] R. G. Stabe, W. J. Whitney, T. P. Moffitt, Performance of a high-work low aspect ratio turbine tested with a realistic inlet radial temperature profile, Technical Memorandum NASA-TM-83655, NASA (June 1984).

[18] N. Cumpsty, Jet Propulsion - A simple guide to the aerodynamic and thermodynamic design and performance of jet engines, Cambridge University Press, 1997, fig. 11.5, p.115.

[19] M. J. Moran, H. N. Shapiro, Fundamentals of engineering thermodynamics, 5th Edition, 2004.

[20] G. P. Anderson, S. A. Clough, F. X. Kneizys, J. H. Chetwynd, E. P. Shettle, Afgl atmospheric constituent profiles (0-120km), Scientific Interim AFGL-TR-86-0110, Air Force Geophysics Laboratory, Hanscom Air Force Base (1986).

[21] J. Etele, M. A. Rosen, Sensitivity of exergy efficiencies of aerospace engines to reference environment selection, Exergy, An International Journal 1 (2) (2001) 91 – 99.

A. Exergy Calculation

The exergy of a pure species X_k has two contributions: the physical exergy and the chemical exergy. The first one is due to changes in its thermo-mechanical state (p, T, v) with respect to the reference environment $(p_0, T_0, 0)$, which in a molar basis can be stated as:

$$\bar{\epsilon}_k^{ph} = \bar{h}_k(p,T) - T_0\bar{s}_k(p,T) + \quad (51)$$

$$+ \quad v^2 \cdot M_k/2 - \bar{g}_k(p_0,T_0). \quad (52)$$

The chemical exergy, in the case of species behaving as semi-perfect gas that are not necessarily present in the environment but produced from the chemical reaction of species present in it, takes the form:

$$\bar{\epsilon}_k^{ch} = \bar{g}_k(p_0,T_0) - \sum_i \nu_{ki}\,\bar{g}_i(y_i^0 \cdot p_0, T_0). \quad (53)$$

In the above expression y_i^0 is the molar fraction of species X_i^0 in the environment and ν_{ki} are the stoichiometric coefficients of the decomposition reaction of one mol of species X_k into the species of the environment $\left\{X_i^0\right\} = \{N_2, O_2, H_2O, Ar\}$:

$$\begin{gathered} N_aO_bH_cAr_d \longrightarrow a/2 \cdot N_2 + \\ +(b/2 - c/4) \cdot O_2 + c/2 \cdot H_2O + d \cdot Ar \end{gathered} \quad (54)$$

$$[\nu_{ki}] = \begin{bmatrix} a_1/2 & b_1/2 - c_1/4 & c_1/2 & d_1 \\ \vdots & \vdots & \vdots & \vdots \\ a_k/2 & b_k/2 - c_k/4 & c_k/2 & d_k \end{bmatrix} \quad (55)$$

The species of the environment and their possible reaction products are at gaseous state, hence the exergy contribution by a possible phase change of the substance to its phase at the current utilization state is accounted by $\bar{\epsilon}_k^{ph}$; the Gibbs potential $\bar{g}_k(p_0, T_0)$ is evaluated for pure gaseous species.

If the fluid stream at pressure p and temperature T consists of an ideal homogeneous mixture of species with molar fractions y_k, then the total exergy can be written as:

$$\bar{\epsilon} = \sum_k y_k \bar{\epsilon}_k^{ph}(y_k \cdot p, T) + \sum_k y_k \bar{\epsilon}_k^{ch} \tag{56}$$

For a constant reference environment, different gas models can be used to evaluate respectively the physical and chemical contributions to the exergy if both provide the same values of enthalpy and entropy at the environmental state (p_0, T_0). It is the case while evaluating the exergy of hydrogen for the present analysis. The chemical contribution is computed from the CEA reference whereas the physical contribution is provided by the more accurate NIST real fluid database. Because the helium does not mix with any other fluid stream, there is no need of computing its chemical exergy, the values shown in Table 2 are the physical exergy contribution. For the air and combustion gases, which are modeled as semi-perfect gases, both exergy contents are evaluated from the CEA reference.

B. Reference Environment

The environment contains the main atmospheric constituents: nitrogen, oxygen, argon and water vapor. Its composition is computed supposing that it behaves as a mixture of steam and dry air such that the volumetric fractions of its constituents are:

$$y_k = (1 - y_w) y_k^{dry};\ k \in \{N_2, O_2, Ar\}, \tag{57}$$

where y_k^{dry} are the mols of N_2, O_2 and Ar per mol of dry air and y_w are the mols of water per mol of dry air. The composition of the dry air is kept constant as the atmospheric conditions p_o, T_o and water content vary: 78.12%, 20.96% and 0.92% in volume of respectively N_2, O_2 and Ar. The water content y_w is specified by means of the relative humidity ϕ, that relates p_o and the saturation pressure of the water at the given environmental temperature T_o:

$$y_w = p_w^v(T_o)/p_o \cdot \phi. \tag{58}$$